Journal of Materials Chemistry A

ROYAL SOCIETY OF CHEMISTRY

PAPER

View Article Online
View Journal

Cite this: DOI: 10.1039/d6ta00823b

Interfacial electrochemistry of Zn anodes in aqueous electrolytes with combined organic cation and halide additives

Sang Hyuk Gong,†[ab] Sunghee Shin, †[ac] Hyo Jin Lim,†[ac] Jin Hwan Kwak,[a] Yiseul Yoo,[ab] In Soo Kim,[d] Puji Lestari Handayani,[e] U. Hyeok Choi, [e] Jae Eun Park, [c] Ji Eun Lee,[c] Seuhg-Ho Yu, [c] Kyung Yoon Chung, [af] Sang Kyu Kwak *[c] and Hyung-Seok Kim *[afg]

Received 28th January 2026
Accepted 7th April 2026

DOI: 10.1039/d6ta00823b

rsc.li/materials-a

Aqueous zinc-ion batteries (AZIBs) have attracted considerable interest as energy storage systems for large-scale applications owing to their low cost, high safety, elemental abundance, and environmental compatibility. However, the Zn metal anode in AZIBs continues to face challenges such as dendrite growth and parasitic side reactions, including hydrogen evolution, corrosion, and byproduct formation. Extensive studies have demonstrated that the electrochemical behavior of Zn anodes during repeated plating and stripping is highly sensitive to electrolyte composition, resulting in pronounced variations in Zn deposition morphology, reversibility, and interfacial stability. Accordingly, electrolyte additives have been widely explored as an effective approach to modulate Zn anode behavior. In this work, we compare the electrochemical responses of Zn anodes in aqueous electrolytes containing quaternary ammonium iodide additives, using tetrabutylammonium iodide (TBAI) as a representative example, over a low concentration range. Particular attention is given to changes in interfacial electrochemical characteristics observed under typical AZIB testing conditions.

1. Introduction

Among the various energy-storage technologies, lithium-ion batteries (LIBs) are the most widely used rechargeable batteries owing to their high energy densities and long lifespans.[1] LIBs have been extensively utilized in portable electronics and electric vehicles; however, they still have some disadvantages such as high flammability, toxicity of organic electrolytes, high prices, and limited lithium resources.[2] Accordingly, multivalent metal-ion batteries have emerged as next-generation secondary batteries.[3] They are particularly promising for grid-scale energy storage systems (ESS) owing to their ability to achieve high volumetric energy densities by the process of transferring multiple electrons with single-ion (de) intercalation at the cathode. Rechargeable aqueous Zn-ion batteries (AZIBs) are emerging as safe and low-cost alternatives to LIBs. Among the multivalent systems (Mg^{2+},[4] Ca^{2+},[5] Al^{3+},[6] Zn), Zn stands out due to its low redox potential (−0.762 V *vs.* SHE) and high theoretical capacity (820 mAh g^{-1}; 5855 mAh cm^{-3}).[7–9] However, the practical deployment of AZIBs is critically hindered by uncontrollable dendritic Zn growth and parasitic side reactions, particularly hydrogen evolution and corrosion. These degradation processes originate from unstable Zn^{2+} deposition dynamics at the electrode–electrolyte interface, resulting in rapid performance decay and limited cycle life.[10–13] Accordingly, both Zn nucleation behavior and the Zn^{2+} solvation environment have been considered important factors influencing the reversibility of Zn plating in aqueous systems.

To address the interfacial instability of Zn metal anodes, a variety of modification strategies have been investigated. Several strategies have been proposed to mitigate the electrochemical instability of Zn anodes in AZIBs. Structural modification approaches, such as dual-channel 3D porous Zn,[8] 3D carbon frameworks,[14] and 3D nanoporous Zn–Cu alloy anodes,[15] have demonstrated improved ion transport pathways

[a]*Energy Storage Research Center, Korea Institute of Science and Technology (KIST), Hwarang-ro 14-gil 5, Seongbuk-gu, Seoul, 02792, Republic of Korea. E-mail: hskim0227@kist.re.kr*

[b]*Department of Materials Science and Engineering, Korea University, 145, Anam-ro, Seongbuk-gu, Seoul, 02841, Republic of Korea*

[c]*Department of Chemical and Biological Engineering, Korea University, 145, Anam-ro, Seongbuk-gu, Seoul, 02841, Republic of Korea. E-mail: skkwak@korea.ac.kr*

[d]*Nonophotonics Research Center, Korea Institute of Science and Technology (KIST), Hwarang-ro 14-gil 5, Seongbuk-gu, Seoul, 02792, Republic of Korea*

[e]*Department of Polymer Science and Engineering and Program in Environmental and Polymer Engineering, Inha University, 100 Inharo, Nam-gu, Incheon, 22212, Republic of Korea*

[f]*Division of Energy & Environment Technology, KIST School, Korea Institute of Science and Technology (KIST), Hwarang-ro 14-gil 5, Seongbuk-gu, Seoul, 02792, Republic of Korea*

[g]*Yonsei-KIST Convergence Research Institute, Yonsei University, 50 Yonsei-ro, Seodaemun-gu, Seoul, 03722, Republic of Korea*

† These authors equally contributed to this work.

and partial suppression of dendrite growth. Interfacial regulation using protective layers, such as sulfur-doped MXene,[16] inorganic–organic hybrid alucone,[17] and Ag coatings,[11] has been shown to facilitate more uniform Zn nucleation, effectively reducing undesirable side reactions between the electrolyte and Zn surface. Beyond direct electrode modification strategies such as surface coating and alloying, several alternative approaches have also been explored to regulate Zn deposition behavior. For instance, separator engineering has been reported to homogenize ion flux and suppress dendrite propagation.[18] Additionally, polymer or gel electrolytes can mechanically constrain Zn deposition and stabilize the electrode–electrolyte interface.[19] Furthermore, rational current collector design has also been demonstrated to guide uniform Zn nucleation and growth.[20]

Compared to these fabrication-intensive strategies, electrolyte additive engineering offers a relatively simple and cost-efficient route.[21–23] Additives such as ethylenediaminetetraacetic acid,[21,22] diethyl ether (Et_2O),[23] polyacrylamide,[24] and ethylene carbonate[25] promote Zn ion redistribution or form shielding interphases that mitigate dendritic formation. Surfactant-type tetrabutylammonium sulfate (TBA_2SO_4),[26] tetraalkylammonium hydroxide,[27] and sodium dodecyl sulfate (SDS)[28] further enhance interfacial reactions through surface adsorption, benefiting deposition morphology control with relatively low toxicity and cost. In addition, chelating agents such as 2-bis(2-hydroxyethyl)amino-2-(hydroxymethyl)-1,3-propanediol[29] and trisodium citrate[30] have been utilized to tailor the Zn^{2+} solvation structure, thereby modulating deposition kinetics and suppressing parasitic reactions. Recent studies have further highlighted that rational electrolyte additive design can effectively regulate Zn deposition behavior and interfacial chemistry in AZIB systems.[31–34] However, many existing additive strategies tend to emphasize either interfacial shielding or solvation modulation, while studies involving combined cation–anion effects often address these aspects independently rather than in an integrated electrochemical context.

The concept of combined cation–anion synergy has recently garnered increasing attention as a strategy to integrate interfacial and solvation regulation in AZIBs. Prior studies employing halide-based ionic liquids,[35,36] concentrated electrolytes,[37] NaI additives[38] or more recent dual-ion cooperative designs[39] have highlighted the potential of ion-pair manipulation for controlling Zn deposition behavior. However, these demonstrations typically rely on comparatively high additive concentrations or specialized electrolyte environments, which can limit their scalability, cost-efficiency, and practical integration into commercial battery systems. The electrochemical responses associated with combined cation–anion effects under dilute electrolyte conditions have not been fully clarified.

In this work, the electrochemical responses of Zn metal anodes in aqueous electrolytes containing quaternary ammonium iodide additives are examined over a low concentration range. Adopting tetrabutylammonium iodide (TBAI) as a representative system, changes in Zn plating/stripping behavior, nucleation overpotential, and interfacial electrochemical characteristics are compared under typical AZIB testing conditions. Rather than aiming to establish definitive mechanistic interpretations, this study focuses on experimentally observable electrochemical trends associated with the presence of organic cation–halide additives. These observations provide a basis for discussing how combined ionic species may influence Zn anode behavior in dilute electrolyte environments.

2. Experimental section

2.1. Preparation of electrolytes containing different concentrations of the TBAI additive

Tetrabutylammonium iodide (Sigma-Aldrich) was dissolved in 2 M $ZnSO_4$ solution (Sigma-Aldrich) until all the TBAI had completely dissolved. The concentrations of TBAI were marked as 2 M $ZnSO_4$ + 0.01 mM TBAI, 2 M $ZnSO_4$ + 0.1 mM TBAI, and 2 M $ZnSO_4$ + 1 mM TBAI, respectively.

2.2. Preparation of the α-MnO_2 cathode

2.2.1. Synthesis of α-MnO_2. The hydrothermal synthesis method was used to produce α-MnO_2.[40,41] Specifically, α-MnO_2 was synthesized by dissolving 0.09878 g of $KMnO_4$ (Junsei) and 0.4226 g of $MnSO_4 \cdot H_2O$ (Sigma-Aldrich) in 80 mL DI water. The resulting solution was then heated at 160 °C for 12 h in a 100 mL Teflon autoclave. After cooling to room temperature, the final α-MnO_2 was obtained by centrifugation, washing with DI water and ethanol, and overnight drying in an 80 °C oven.

Active materials (as-synthesized α-MnO_2), Super-P (MTI Korea), and PVDF (Sigma-Aldrich) in a weight ratio of 70 : 20 : 10 in *N*-methyl-2-pyrrolidone (NMP, Daejung) were mixed by using a mini-mill (Mini-Mill PULVERISETTE 23, Fritsch). Then, the α-MnO_2 slurry was coated on titanium foil (Alfa Aesar) using a doctor blade. After overnight drying in an 80 °C oven, the α-MnO_2 cathode was punched into 14 pi with a mass loading of 2–2.5 mg cm^{-2}.

2.3. Preparation of the ZVO cathode

2.3.1. Synthesis of ZVO ($Zn_xV_2O_5 \cdot nH_2O$) nanobelts. The hydrothermal synthesis method was used to synthesize ZVO nanobelts.[42,43] 2 mmol V_2O_5 (98%; Sigma-Aldrich) and 1.3 mmol $Zn(CH_3COO)_2 \cdot 2H_2O$ (98%; Sigma-Aldrich) were added and stirred in 50 mL water/acetone solution with a volume ratio of 15 : 1. The resulting solution was then transferred into a 100 mL Teflon autoclave and heated at 180 °C for 9 h. The final ZVO nanobelts were obtained by centrifugation, washing with DI water 4 times, and overnight drying in an 80 °C oven.

The ZVO slurry (composed of a 70 : 20 : 10 wt% ratio of active materials (synthesized ZVO nanobelts): MWCNT (CNT MR99, Carbon-Nanotech): PVDF (Sigma-Aldrich) in *N*-methyl-2-pyrrolidone (NMP, Daejung)) was mixed by using a Thinky mixer (THI ARM-310, Intertronics) and coated on titanium foil (Alfa Aesar) using a doctor blade. Finally, the ZVO cathode was obtained after drying in an 80 °C oven for at least 12 h. The mass loading of the ZVO cathode was about ~1 mg cm^{-2}.

2.4. Computational calculations

Quantum chemistry calculations were carried out with the Gaussian 09 software package to obtain the binding energies of TBA^+–H_2O, Zn^{2+}–H_2O, TBAI–H_2O, $Zn(H_2O)_6^{2+}$, and $ZnI(H_2O)_5^+$. The geometry optimization, the energy calculation, and the LUMO–HOMO energy level were also performed with the 3-parameter hybrid Becke exchange/Lee–Yang–Parr (B3LYP) density functional theory. For a more accurate description, a double zeta basis set (LANL2DZ) was used for iodine and a 6-31G(2d,2p) basis set was applied to the other atoms. The binding energies of Zn^{2+}–H_2O and the other molecules were calculated using the following equation:

$$E_b = E_{tot\ complex} - E_{Zn^{2+}} - E_{H_2O}$$

where E_b is the binding energy (kcal mol^{-1}), $E_{tot\ complex}$ is the total energy of the optimized structure for complex molecules, and $E_{Zn^{2+}}$ and E_{H_2O} are the energy of Zn^{2+} and H_2O, respectively.

Based on the Zn^{2+} solvation structures analyzed from the MD simulations, model structures were constructed to calculate the activation energies associated with structural transitions. In particular, to compare the transition possibilities from solvent-shared ion pair (SIP) and solvent-separated ion pair (SSIP) structures to contact ion pair (CIP) structures, initial configurations representing each reaction pathway were selected based on the predominant coordination structures identified from MD analyses.

DFT calculations were performed to optimize components of the electrolyte system and to evaluate the activation energy for the transition from SIP and SSIP to CIP structures, obtained from the MD simulation results. All DFT calculations were carried out using the DMol3 program.[44,45] The B3LYP hybrid functional was utilized for all calculations.[46,47] The spin-polarized calculation was performed with the DNP 4.4 level. All electron relativistic effects were included in the core treatment. The convergence criterion for the self-consistent field was set to 1.0×10^{-6} eV per atom. For geometry optimization, the convergence criteria were set as 1.0×10^{-5} Ha for energy, 0.002 Ha $Å^{-1}$ for force, and 0.005 Å for displacement, respectively. For transition state calculations, the complete single linear synchronous transit and quadratic synchronous transit methods were employed, with the convergence criterion for the root mean square force set as 0.003 Ha $Å^{-1}$.

2.5. Materials characterization

Scanning electron microscopy (SEM, Inspect F and Regulus 8230) was used to observe the morphology of Zn dendrites from both the top-view and cross-section view perspectives. An atomic force microscope (AFM, XE-100) was utilized to directly identify the mechanism of nucleation and growth of Zn dendrites. The electrochemical Zn deposition morphology was directly observed using a CMOS 8M camera (E3ISPM08300KPA, HiMax Tech, Korea) connected to an optical microscope (HNM001, HiMax Tech, Korea). Changes in the crystalline structure of Zn foil after soaking in different electrolytes were analysed by X-ray diffraction (XRD, Bruker D8 ADVANCE diffractometer) with a Cu Kα source (1.5418 Å) at 40 kV and 40 mA. The ^1H NMR spectrum was recorded using an AscendTM 400 MHz NMR. The Raman spectra were obtained by using an Alpho300R spectrometer (WITec) under ambient conditions. A 532 nm laser was used as a light source to excite samples at a power of ~2 mW cm^{-2}.

2.6. Electrochemical measurements

Zn‖Zn symmetric cells, Zn@MnO_2, and Zn@ZVO full cells were assembled in CR2032-type coin cells to evaluate electrochemical performance. Symmetric cells were fabricated using Zn foil (Alfa Aesar) as both the working and counter electrodes, and glass-fiber F (Whatman) as the separator. For full cells, MnO_2 and ZVO cathodes were paired with Zn foil anodes.

The Zn‖Zn symmetric cell's galvanostatic charge/discharge tests were performed using a WonATech galvanostat at current densities of 2, 5, and 10 mA cm^{-2} with areal capacities of 1, 5, and 10 mAh cm^{-2}, respectively.

Chronoamperometry (CA; Bio-Logic VMP3) was conducted by applying a potential of −150 mV. Electrochemical impedance spectroscopy (EIS) was performed with an AC perturbation of 0.1 mV over the frequency range of 1 MHz to 0.1 Hz using the same instrument, and Nyquist plots were fitted using EC-Lab software.

To calculate the Zn^{2+} transference number, the Bruce–Vincent–Evans method was adopted. CA was conducted at −10 mV for Zn‖Zn symmetric cells until a steady-state current was achieved. Subsequently, EIS was conducted under the same frequency conditions. The transference number t_+ was calculated using the equation:

$$t_+ = \frac{I_{ss}(\Delta V - I_0 R_0)}{I_0(\Delta V - I_{ss} R_{ss})}$$

where I_0 and I_{ss} are the initial and steady-state currents, respectively, and R_0 and R_{ss} are the interfacial resistances obtained from EIS before and after CA measurement, respectively. Tafel polarization and cyclic voltammetry (CV) were carried out in a three-electrode configuration, with Zn foil as the working electrode, carbon as the counter electrode, and calomel as the reference electrode. CV was conducted at a scan rate of 0.1 mV s^{-1}. Linear sweep voltammetry (LSV) was also conducted in a three-electrode setup using Pt foil as both the working and counter electrodes, Ag/AgCl as the reference electrode, and a scan rate of 1 mV s^{-1} to evaluate the onset potential of the hydrogen evolution reaction (HER). To assess HER suppression, internal pressure monitoring and differential electrochemical mass spectrometry (DEMS) were conducted using a custom-designed 2032 type coin cell (hereafter referred to as the HS cell). For the internal pressure test, the HS cell was maintained in a closed state for 7 days. The resulting internal pressure change was used to estimate H_2 gas generation. DEMS analysis was subsequently carried out using the same HS cell configuration to quantify HER behavior in Zn@MnO_2 full cells with different types of electrolytes, with or without TBAI additives. A SUS mesh was incorporated to enable uniform gas delivery and argon was used as a carrier gas in the HS cell. After purging the

residual air inside the HS cell with argon for 30 minutes, the cell was sealed and maintained in a closed state for 10 hours. The accumulated gas was then released and analyzed *via* the argon carrier line to evaluate H_2 generation due to side reactions.

3. Results and discussion

3.1. Zn dendrite suppression effect of TBAI

To assess the electrochemical impact of TBAI, a Zn‖Zn symmetric cell was fabricated. Fig. 1 shows the voltage profiles of the symmetric cells at different current densities and specific capacities. As indicated in Fig. 1a, symmetrical Zn cells exhibited different long-term cycling behaviors depending on the presence and concentration of TBAI in the electrolyte. The cell employing the baseline electrolyte (2 M $ZnSO_4$) exhibited a short-circuit after 215 h, while cells containing 1 mM and 0.1 mM TBAI showed a short-circuit after 121 h and 380 h, respectively. Remarkably, the cell with 0.01 mM TBAI in the baseline electrolyte exhibited enhanced cycling stability, operating without failure for over 1500 h. These results indicate that the cycling behavior of the Zn symmetric cell is sensitive to the additive concentration. In this system, a low concentration of TBAI (0.01 mM) showed the most stable behavior among the tested concentrations. To examine the effect of TBAI concentration in detail, we analyzed the cycle plating/stripping voltage profiles (Fig. S1a–d, SI). The overpotential (ΔV) of the first cycle increased from 80.3 mV for the baseline electrolyte to 84.6 mV with 0.01 mM TBAI, and further to 155.1 mV and 267.2 mV for 0.1 mM and 1 mM, respectively. The pronounced increase in overpotential at higher additive concentrations may be associated with hindered Zn^{2+} transport and altered interfacial kinetics in the presence of excess TBA^+. Over prolonged cycling, the baseline electrolyte showed a gradual increase in polarization, indicating worsening reversibility of Zn plating/stripping

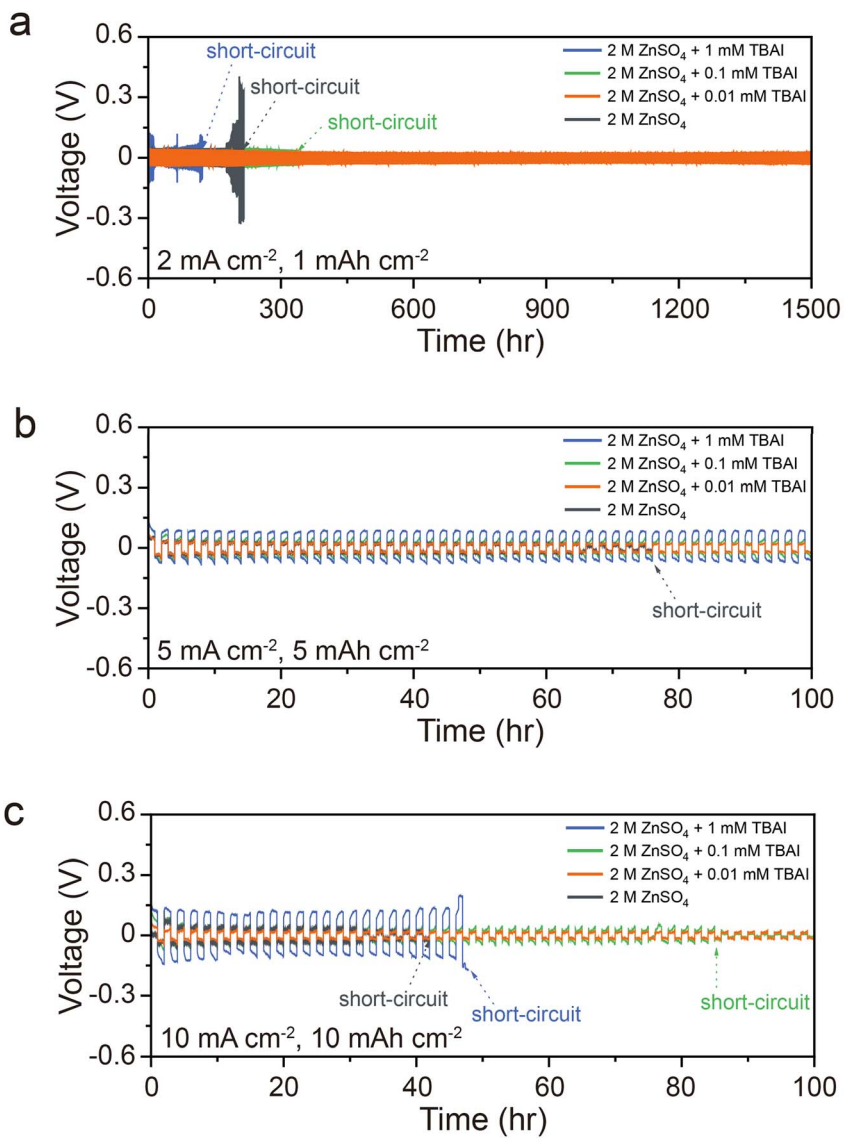

Fig. 1 Voltage profile of Zn symmetric cells according to TBAI concentration at a current density of (a) 2 mA cm^{-2} with a capacity of 1 mAh cm^{-2}, (b) 5 mA cm^{-2} with a capacity of 5 mAh cm^{-2} and (c) 10 mA cm^{-2} with a capacity of 10 mAh cm^{-2}.

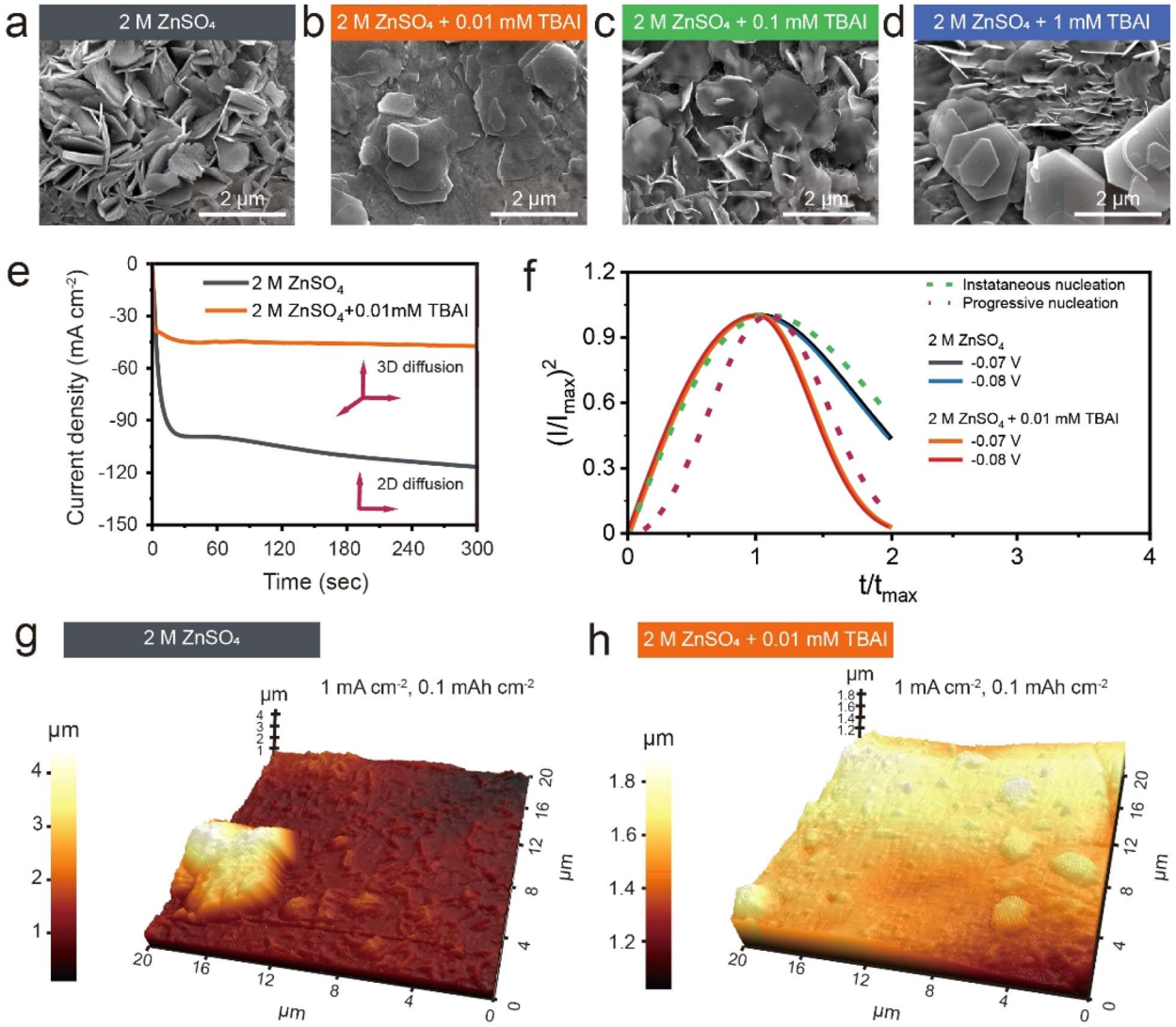

Fig. 2 SEM images of the Zn surface of a symmetric cell after 50th cycles in (a) bare and with (b) TBAI 0.01 mM, (c) TBAI 0.1 mM, and (d) TBAI 1 mM. (e) CA curves of zinc in each electrolyte. (f) Dimensionless curves (I/I_{max}) *vs.* (t/t_{max}) for instantaneous and progressive nucleation from eqn (S1) and (S2), respectively (dotted lines) along with experimental data. AFM images of Zn surface after plated at current density of 1 mA cm^{-2} and a specific capacity of 0.1 mAh cm^{-2} in (g) no add and (h) with 0.01 mM TBAI.

and surface instability. Conversely, the cell with 0.01 mM TBAI maintained a relatively stable voltage profile, suggesting suppressed overpotential growth and improving Zn plating/stripping kinetics over extended cycles (Fig. S1e and f, SI). To verify this trend under more demanding conditions, the current density and areal capacity were increased. When the current density and specific capacity increased to 5 mA cm^{-2} and 5 mAh cm^{-2} (Fig. 1b), respectively, the cells containing TBAI (0.01 mM, 0.1 mM, and 1 mM) exhibited a stable and reversible plating/stripping process for 50 cycles (100 h). In contrast, the cell without TBAI failed after 33 cycles (66 h). At a current density of 10 mA cm^{-2} and a specific capacity of 10 mAh cm^{-2} (Fig. 1c), the cell without TBAI short-circuited only after 16 cycles (32 h). Even the cells containing 1 mM and 0.1 mM TBAI short-circuited in the 23rd cycle (46 h) and 43rd cycle (86 h), respectively. Notably, the cell with 0.01 mM TBAI exhibited a stable voltage profile with the lowest polarization over 50 cycles (100 h). The Zn||Cu asymmetric cell test was conducted for more detailed insight into the Zn deposition/stripping process (Fig. S2, SI). From the initial cycles, the electrolyte with 0.01 mM TBAI exhibited a remarkably high coulombic efficiency (CE) of 99.8%, whereas the CE of the electrolyte without TBAI reached only 98.25% even after 20 cycles. These results indicate that the presence of 0.01 mM TBAI is associated with improved reversibility of the Zn deposition/stripping process and improves cycling stability. To assess the impact of TBAI concentration on Zn plating morphology, SEM images were collected after 50 cycles at 1 mA cm^{-2} and 0.1 mAh cm^{-2} (Fig. 2a–d). In 2 M $ZnSO_4$ without TBAI (Fig. 2a), the Zn surface was covered with numerous vertically growing flakes, indicative of dendrite growth. In contrast, TBAI-containing cells exhibited a stacked plate-like morphology (Fig. 2b–d). Previous studies have suggested that bulky TBA^+ cations can preferentially interact with protruding regions of the Zn surface during plating.[26] In our study, the number of

vertically grown flakes increased as the concentration of TBAI increased on the surface of Zn after cycles, suggesting that excess TBA^+ cations may interact with both protruding and flat regions, hindering preferential Zn plating on the flat region of the Zn. In this context, the morphology observed at different TBAI concentrations may reflect variations in surface coverage and local deposition behavior. This corresponds to only 0.00037 g L^{-1}, lower than that of previously reported additives (Table S1, SI). This comparison suggests that the combined presence of I^- ions and TBA^+ is associated with enhanced cycling stability under the examined conditions.[26] To examine the individual contributions of I^- anions and TBA^+, additional symmetric cell tests were conducted in environments containing 0.01 mM I^- and 0.01 mM TBA^+ alone (Fig. S3, SI). Among the tested electrolytes (2 M $ZnSO_4$, 2 M $ZnSO_4$ + 0.01 mM ZnI_2, 2 M $ZnSO_4$ + 0.005 mM TBA_2SO_4, and 2 M $ZnSO_4$ + 0.01 mM TBAI), 2 M $ZnSO_4$ + 0.01 mM TBAI exhibits the most stable cycling behavior. This result suggests that the combined presence of TBA^+ and I^- is associated with enhanced cycling stability under the examined conditions, and more in-depth discussion will be presented in a later section.

The chronoamperometry (CA) test was conducted to verify the effect of a representative low TBAI concentration (0.01 mM) on Zn nucleation and growth processes at an overpotential of 150 mV in Zn symmetric cells and the results are shown in Fig. 2e. In the CA results, the fluctuations in the current–time curve sensitively reflect the nucleation, nuclei growth, and surface morphology changes.[48] The initial rapid decrease in current may be associated with nucleation. As shown in Fig. S4, the symmetric cell with 2 M $ZnSO_4$ and 0.01 mM TBAI exhibited a shorter nucleation time than a symmetric cell without a TBAI additive. The shortened nucleation time observed in the presence of 0.01 mM TBAI suggests a modified nucleation process, which may be related to changes in the interfacial environment induced by the additive.[30] This is closely related to the difference in desolvation energies for Zn ions depending on the existence of additives and this will be discussed in more detail in the subsequent section. Previous studies have suggested that Zn nuclei formed after nucleation can grow *via* either 2D or 3D diffusion-controlled processes.[49–52] In 2D diffusion, adsorbed Zn^{2+} ions migrate laterally to energetically favorable sites, generating large nuclei and promoting dendrite growth. In contrast, 3D diffusion involves local reduction of Zn^{2+} with minimal lateral migration, limiting nuclei growth and suppressing dendrites. The continuous increase in absolute current density indicates dominant 2D diffusion. In our study, the TBAI-free cell showed such an increase, whereas the cell with 0.01 mM TBAI maintained a steady current density (Fig. 2e), indicating predominant 3D diffusion. Collectively, these observations are consistent with a transition toward more uniform Zn nucleation and growth behavior in the presence of 0.01 mM TBAI. To further understand Zn nucleation and growth, we used Scharifker and Hill's model, which is classified into two cases (*i.e.*, instantaneous nucleation and progressive nucleation).[53] The *I–t* transient curves for each electrolyte, measured to construct the Sharifker and Hill's model curve, are presented in Fig. S5a and b. These figures demonstrate that the addition of 0.01 mM TBAI to the bare electrolyte constrains surface diffusion of Zn during the nucleation process, consistent with the CA results. To facilitate comparison, we normalized the *I–t* curves to (I/I_{max})–(t/t_{max}) and plotted them alongside theoretical curves based on Scharifker and Hills' model (eqn (S1) and (S2), SI), as shown in Fig. 2f. According to this model, nucleation occurring rapidly at a small number of active sites is classified as "instantaneous nucleation," whereas nucleation occurring more gradually across a large number of active sites is referred to as "progressive nucleation". It is well established that progressive nucleation promotes uniform nuclei growth, thereby mitigating Zn dendritic growth. Our results indicate that the transient curve for the bare electrolyte closely follows the instantaneous nucleation model, whereas the curve corresponding to the 0.01 mM TBAI-containing electrolyte aligns more closely with the progressive nucleation model. This observation is consistent with the formation of more uniformly distributed Zn nuclei in the presence of 0.01 mM TBAI.

To better understand the effect of TBAI on Zn nucleation and early-stage growth, AFM measurements were performed. As shown in Fig. 2g, Zn plated without TBAI exhibited highly non-uniform surface features with large particulate-like protrusions, indicative of localized and inhomogeneous deposition. In contrast, the Zn surface plated with TBAI (Fig. 2h) showed finer and more uniformly distributed particulates with smaller local height variations, suggesting more homogeneous Zn nucleation and growth during the initial deposition process. It should be noted that AFM provides localized surface topography rather than an exact measurement of overall film thickness; nevertheless, the results clearly demonstrate the role of TBAI in promoting uniform Zn electrodeposition. To investigate the plating over a wider area, SEM analysis was performed, as shown in Fig. 3a and b. Even in a wide range of space, the Zn surface after plating without TBAI exhibited numerous larger particulates on the surface compared to those on the surface after plating with TBAI. To observe the initial Zn plating process in real-time more directly, *in situ* OM for Cu||Zn asymmetric cells in bare electrolyte and 0.01 mM TBAI-added electrolyte was conducted under the same plating conditions as those for AFM and SEM. The results (Videos S1 and S2, SI) show that the Zn nucleation occurred more evenly in the TBAI-added electrolyte than in the bare electrolyte during the initial plating process. These results support the findings from the previously discussed Sharifker and Hill's model and CA test, evidencing that the TBAI-containing electrolyte promotes a large number of nucleation sites and uniform 3D diffusion-driven Zn growth. To examine the effect of 0.01 mM TBAI associated with suppressed dendritic growth beyond the nucleation stage, cross-sectional images of the Zn anode were acquired after plating (Fig. 3a and b). Without TBAI, the Zn layer consisted of agglomerated particulates ~40 μm thick, indicative of dendritic growth (Fig. 3a). In contrast, 0.01 mM TBAI yielded a dense, uniform Zn layer only 7 μm thick (Fig. 3b), confirming effective dendrite suppression *via* compact deposition. To further elucidate this effect, *in situ* cross-sectional OM was conducted at a current density of 5 mA cm^{-2}. In 2 M $ZnSO_4$, protrusions started to appear on the Zn surface after 30 min of plating (Fig. 3c). Such

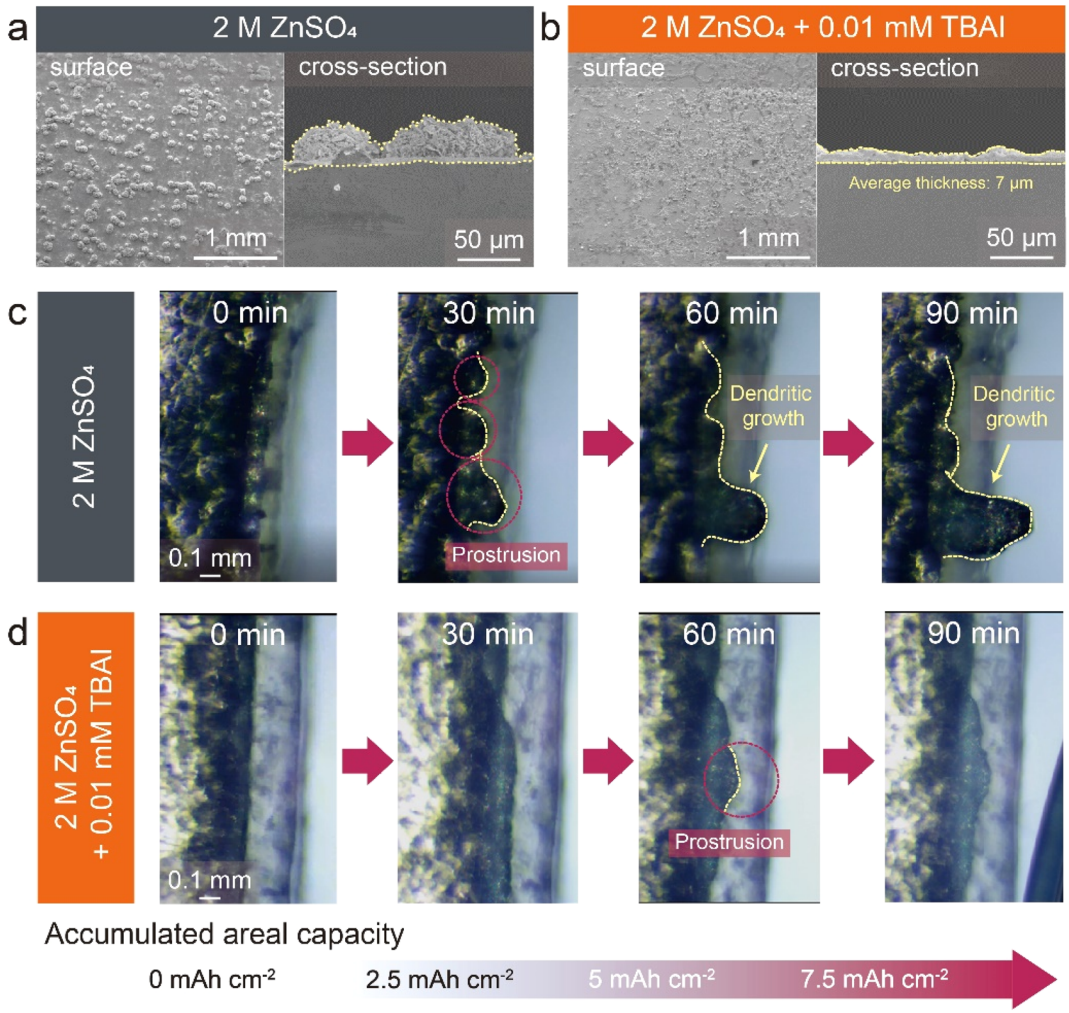

Fig. 3 SEM images (top view and cross section) of Zn surface of beaker cell with only deposition at current density of 1 mA cm^{-2} for 2 h in (a) 2 M $ZnSO_4$ and (b) 2 M $ZnSO_4$ with TBAI 0.01 mM. *In situ* optical microscopy images during the plating process in (c) 2 M $ZnSO_4$ and (d) 2 M $ZnSO_4$ with TBAI 0.01 mM.

protrusions typically accelerate dendritic growth owing to the tip effect.[53] Consequently, the largest protrusion continued growth after 90 min. In contrast, 2 M $ZnSO_4$ with 0.01 mM TBAI produced a uniform, compact Zn surface within 30 min (Fig. 3d), which remained dendrite-free even after 90 min. These observations further support the trends observed in the CA and nucleation analyses. To further evaluate whether such stabilized deposition behavior can be maintained under practical operating conditions, symmetric cells were tested at various current densities (Fig. S7). The TBAI-containing electrolyte exhibits significantly reduced polarization and stable voltage profiles even at high current densities, indicating that the suppressed dendritic growth translates into enhanced interfacial stability and improved Zn plating/stripping reversibility.

3.2. Suppression of side reactions by the TBAI additives

In addition to the dendritic growth, Zn anodes in AZIBs suffer from various side reactions (zinc corrosion, hydrogen evolution, and anode passivation). To probe the effect of TBAI, electrochemical and physicochemical analyses were performed. Electrochemical impedance spectroscopy (EIS, Fig. 4a–c) revealed that while the TBAI-containing electrolyte initially showed a slightly larger semicircle than bare $ZnSO_4$, its interfacial resistance remained far more stable over 7 days of rest, indicating suppressed corrosion and byproduct accumulation (see fitting details in Fig. S8, SI). This behavior suggests that the presence of TBAI is associated with mitigated interfacial degradation, potentially due to altered surface interactions. The corresponding Bode plots show similar stabilization trends (Fig. S9, SI).[29] To further verify the anticorrosion capability of TBAI, Tafel polarization and cyclic voltammetry (CV) analyses were conducted. As shown in the Tafel curves (Fig. S10, SI), adding 0.01 mM TBAI to 2 M $ZnSO_4$ shifted the corrosion potential positively and reduced the corrosion current from 2.49 mA to 1.89 mA (Table S2, SI), consistent with a reduced corrosion tendency.[27] CV profiles (Fig. S11, SI) revealed only the characteristic Zn plating/stripping peaks in both electrolytes, with decreased peak currents upon TBAI addition, suggesting suppressed corrosion and reduced byproduct accumulation.[54] CV of 0.01 mM TBAI in water (without 2 M $ZnSO_4$) shows no

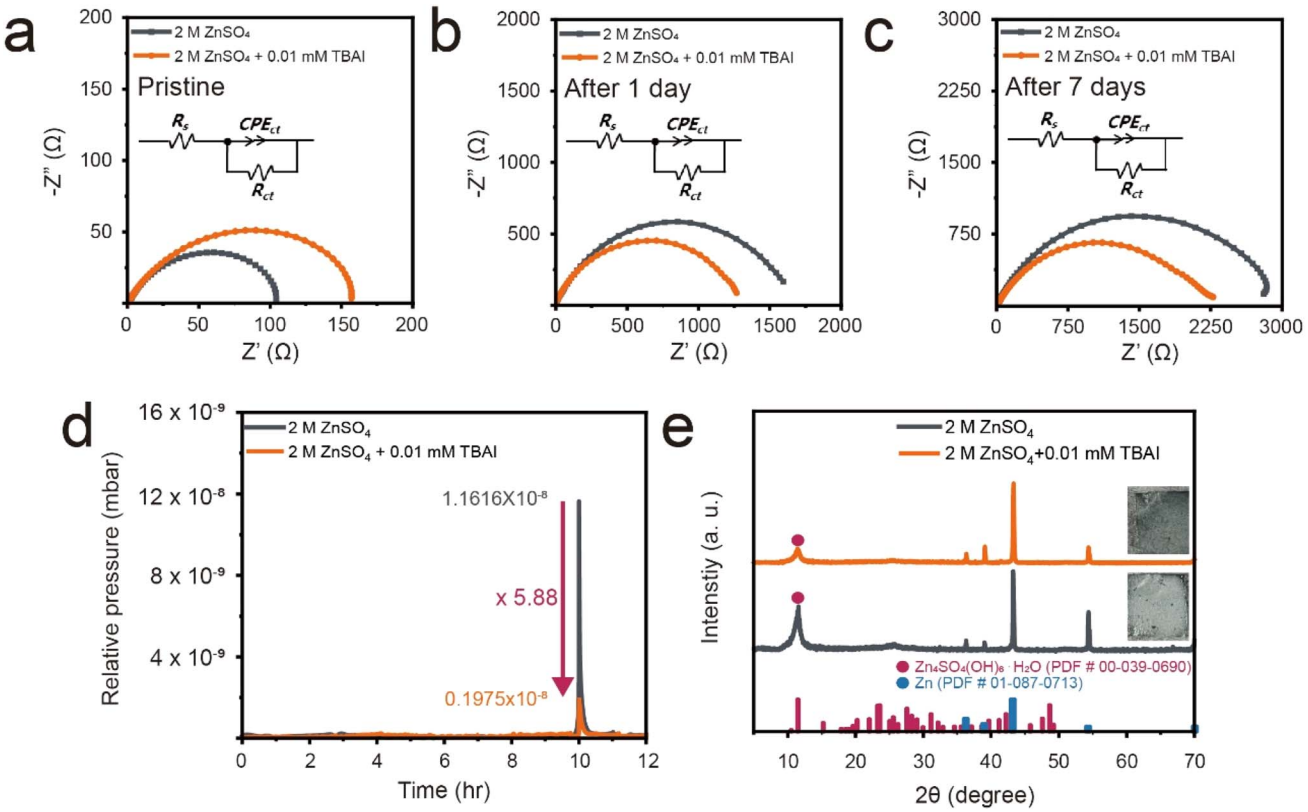

Fig. 4 Electrochemical impedance spectroscopy (EIS) and side reaction analyses of Zn symmetric cells in 2 M $ZnSO_4$ electrolyte with and without 0.01 mM TBAI additive. (a) Nyquist plots of pristine Zn||Zn cells. (b) Nyquist plots after 1 day rest. (c) Nyquist plots after 7 days rest. Inset in (a)–(c) is the equivalent circuit model used for fitting. (d) Time-resolved differential electrochemical mass spectroscopy analysis (DEMS) for quantifying H_2 gas generation during rest. (e) XRD patterns of Zn after soaking for 7 days in different electrolytes. Insets show optical images of the Zn surfaces after soaking.

distinct peaks, confirming that TBAI is electrochemically inert during Zn plating/stripping. The effect of TBAI on hydrogen evolution reaction (HER) suppression was further investigated by linear sweep voltammetry (LSV, Fig. S12, SI). The onset potential for the HER shifted positively from −1.02 V to −0.99 V *vs.* Ag/AgCl upon TBAI addition, suggesting suppressed HER kinetics. This result was corroborated by internal pressure monitoring in HS cells over seven days. Pressure changes were tracked in both half-cell systems (bare Zn, without an additive) and full-cell systems (Zn@MnO_2, with/without an additive) (Fig. S13, SI). In additive-free systems, the internal pressure increased continuously, reaching 15.2 psi for bare Zn and 14.2 psi for Zn@MnO_2 after one week. In contrast, the Zn@MnO_2 cell containing 0.01 mM TBAI showed a significantly lower internal pressure of 6.2 psi, representing a >50% reduction compared with additive-free cells. To quantitatively assess HER inhibition, differential electrochemical mass spectrometry (DEMS) was employed. After a 10 h resting period, the relative hydrogen gas pressure of the additive-free electrolyte was 1.1616 $\times 10^{-8}$ mbar, whereas that of the 0.01 mM TBAI electrolyte was reduced by 5.88-fold to 0.1975 $\times 10^{-8}$ mbar (Fig. 4d). These results indicate that the presence of 0.01 mM TBAI is associated with reduced HER under the examined conditions. In AZIBs, the HER also generates side reactants, such as zinc hydroxide sulfate (ZHS), which impedes reversible Zn plating/stripping and are closely associated with corrosion and hydrogen evolution.[48] To evaluate the effect of TBAI on ZHS formation, pieces of Zn foil were soaked in each electrolyte for seven days. The XRD patterns (Fig. 4e) revealed that ZHS formation was significantly suppressed in 2 M $ZnSO_4$ containing 0.01 mM TBAI compared with the additive-free electrolyte. Consistently, the Zn surface morphology after soaking (inset, Fig. 4e) exhibited abundant gray by-product deposits in the absence of TBAI,[55] whereas substantially fewer deposits formed in the TBAI-containing electrolyte. Additional SEM and EDS mapping images (Fig. S14, SI) further support that the presence of 0.01 mM TBAI is associated with suppressed ZHS formation.

Collectively, the electrochemical and post-mortem analyses indicate that the presence of TBAI is associated with reduced corrosion, suppressed hydrogen evolution, and mitigated byproduct formation under the examined conditions.

3.3. Effect of TBAI on the solvation structure of Zn^{2+} ions

While these observations highlight the influence of TBAI on interfacial side reactions, the observed electrochemical improvements cannot be fully explained by interfacial effects alone. Given the strong dependence of Zn deposition behavior on the solvation environment, the influence of TBAI on Zn^{2+} solvation was further examined using spectroscopic and

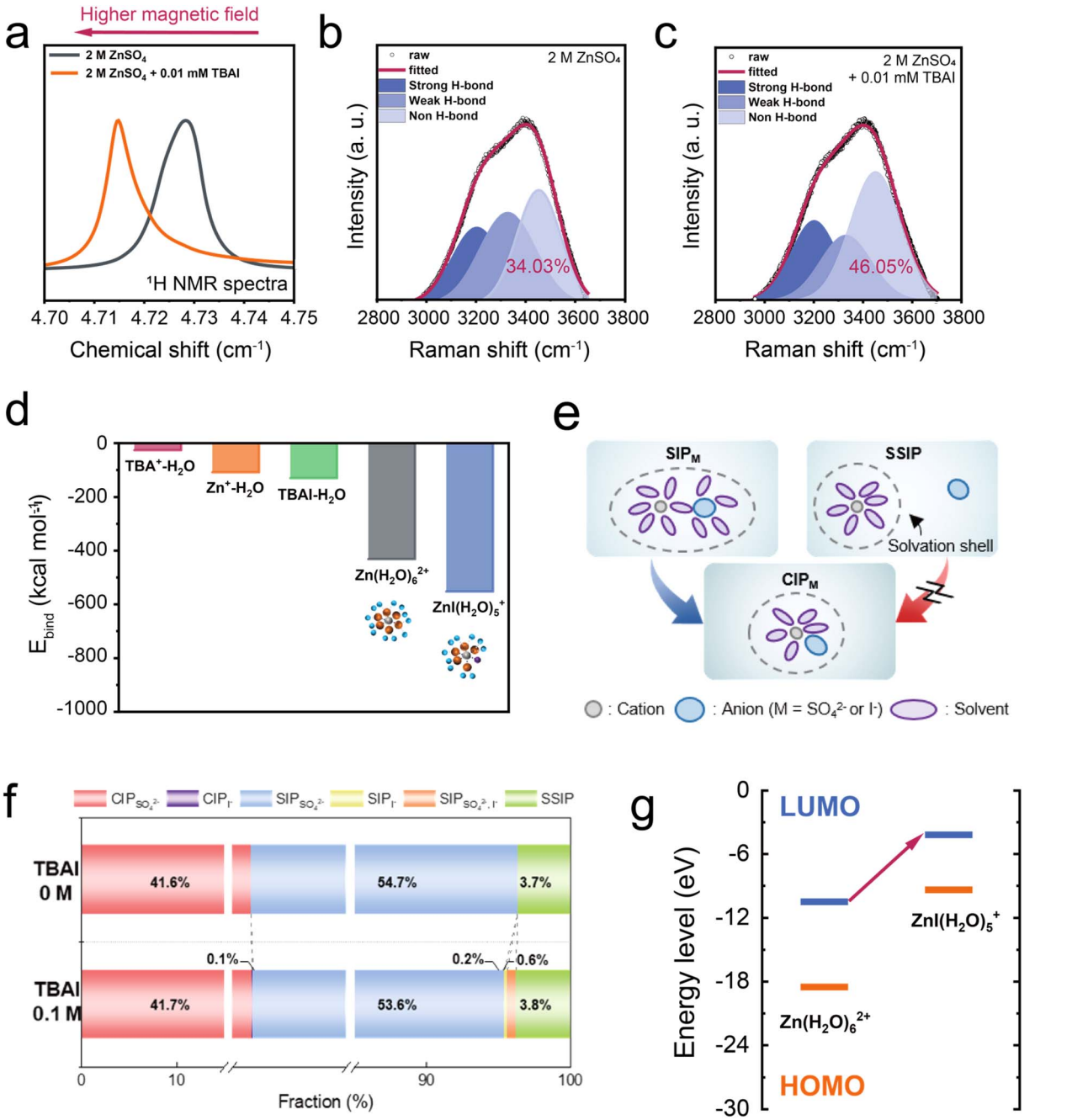

Fig. 5 (a) ^{1}H NMR spectra of electrolytes. The fitted O–H stretching vibration of Raman spectra representing water molecules with strong, weak, and non H-bonds in (b) 2 M $ZnSO_4$ and (c) 2 M $ZnSO_4$ + 0.01 mM TBAI. (d) The calculated binding energy between ions and water, and the formation energies of Zn^{2+} solvation configurations. (e) Schematic illustration of solvation structure transition. (f) Fraction of the solvate species (contact ion pairs [CIPs], solvent-shared ion pairs [SIPs], and solvent-separated ion pairs [SSIPs]) with varying TBAI concentrations of the 2 M $ZnSO_4$ electrolytes. (g) The calculated HOMO and LUMO energy level of Zn^{2+} solvation configurations.

computational approaches. In general, electrolyte additives inevitably alter the solvation structure of Zn^{2+} ions, which is one of the major factors influencing reactions in the AZIB system. To investigate these changes, we conducted an NMR analysis of both electrolytes. In 2 M $ZnSO_4$, the ^{1}H peak appeared at 4.728 ppm, shifting to 4.715 ppm upon TBAI addition (Fig. 5a), suggesting subtle changes in the local hydration environment of Zn^{2+} and weakened Zn^{2+}–H_2O interactions.[55] To further investigate the interaction between the H_2O molecules and Zn^{2+}, Raman spectroscopy was performed. Raman spectra (Fig. 5b and c) show a broad O–H stretching band (2900–3700 cm^{-1}) deconvoluted into peaks for strongly, weakly, and non-H-bonded water.[56] To quantitatively assess the distribution of water in various hydrogen-bonded states, we calculated ratios of the areas of the fitted Raman peaks (Fig. S15, SI). The non-H-bonded fraction increased from 34.03% to 46.05% with TBAI, suggesting that the addition of 0.01 mM TBAI to 2 M $ZnSO_4$ is associated with redistribution of hydrogen-bonded water

species around Zn^{2+}, with an increased fraction of free H_2O molecules. To assess the impact of changes in the solvation structure on Zn^{2+} transport, the Zn^{2+} transference number ($t_{Zn^{2+}}$) was measured (Fig. S16, SI). The transference number was determined *via* chronoamperometry, and the corresponding impedance spectra (insets). The value ($t_{Zn^{2+}}$) increased from 0.582 (2 M $ZnSO_4$) to 0.655 with TBAI, suggesting a modest change in Zn^{2+} transport behavior under the examined conditions.[57] Previous studies suggested that bulky cations can be incorporated into the solvation structure $[Zn(H_2O)_6]^{2+}$, leading to improved electrochemical properties.[58–61] However, 2 M $ZnSO_4$ containing 0.01 mM TBAI exhibits higher cycling stability than the electrolyte containing only TBA^+, indicating that an additional factor beyond the bulky cation affects the solvation structure and Zn^{2+} plating behavior (Fig. S3 and Table S1, SI). Thus, we hypothesized that I^- also plays a role in modifying the Zn^{2+} solvation structure and performed related density functional theory (DFT) calculations to verify this.58 The calculated binding energy of TBA^+–H_2O (-26.136 kcal mol^{-1}) is much weaker than that of Zn^{2+}–H_2O (-108.768 kcal mol^{-1}) (Fig. S17, SI). This suggests that direct coordination between TBA^+ and Zn^{2+} is unlikely to be a dominant factor in modifying the Zn^{2+} solvation structure. Further DFT calculations were performed to examine the coordination environment of I^- and the solvated Zn structure (Fig. 5d). The binding energy of $[Zn(H_2O)_6]^{2+}$ (-431.438 kcal mol^{-1}) was stronger than those of TBA^+–H_2O, Zn^{2+}–H_2O, and TBAI–H_2O in the water system, indicating that $[Zn(H_2O)_6]^{2+}$ is the general solvation structure in water. Interestingly, the binding energy of $ZnI(H_2O)_5^+$ (-552.208 kcal mol^{-1}) was stronger than that of $[Zn(H_2O)_6]^{2+}$ in the water system suggesting that $ZnI(H_2O)_5^+$ is thermodynamically feasible in I^- rich local environments, although the population of such species under dilute conditions is expected to be limited.

To explicitly examine the effect of TBAI in the aqueous Zn electrolyte system, molecular dynamics (MD) simulations were performed (see Section 2.4. Computational calculations under the Experimental section). Changes in solvation species induced by the additives were analyzed by examining the Zn^{2+} solvation structures in the electrolytes without TBAI and with 0.1 M TBAI. It should be noted that the additive concentration employed in the MD simulations is higher than that used in the experiments, which was adopted to enhance statistical sampling of solvation structures (Fig. S17, SI). Under trace-level additive conditions, the number of additive molecules within a finite simulation box becomes extremely limited, making it difficult to obtain statistically meaningful structural information within accessible simulation times. Therefore, the MD results are used to qualitatively illustrate possible trends in solvation behavior rather than to quantitatively reproduce the experimental electrolyte composition. The results are presented in Fig. 5f. The solvation structure species of Zn^{2+} are categorized into $CIPI^-$ (*i.e.*, $ZnI(H_2O)_5^+$), $CIPSO_4^{2-}$ (*i.e.*, $ZnSO_4(H_2O)_5$), $SIPSO_4^{2-}$ (*i.e.*, $[Zn(H_2O)_5\cdots H_2O\cdots SO_4^{2-}]$), $SIPI^-$ (*i.e.*, $[Zn(H_2O)_5\cdots H_2O\cdots I^-]^+$), $SIPSO_4^{2-}$, I^- (*i.e.*, $[Zn(H_2O)_4\cdots H_2O\cdots SO_4^{2-}$ and $H_2O\cdots I^-]^-$), and SSIP (*i.e.*, $Zn(H_2O)_6^{2+}$). In the presence of TBAI, a slight increase in CIP structures was observed compared to the additive-free system, including a minor contribution of the $CIPI^-$ structures (*i.e.*, purple) as expected from the DFT calculation (Fig. 5d). Also, the population of $SIPSO_4^{2-}$ decreased, while $SIPI^-$, $SIPSO_4^{2-}$, or I^-, emerged (*i.e.*, blue, yellow, and orange, respectively). To further understand the SIP structure formation, radial distribution function (RDF) analysis between SO_4^{2-} and H_2O revealed a subtle peak shift toward longer distances upon TBAI addition (Fig. S19, SI). Such a peak shift caused by the existence of TBAI indicates a weakening of SO_4^{2-} and H_2O interaction, suggesting that SO_4^{2-} becomes less competitive in forming SIP structures, thereby increasing the relative likelihood of I^- serving as the SIP-forming anion. These findings suggest that the presence of TBAI can influence the local Zn^{2+} solvation environment by altering the relative populations of anion-associated solvation structures.[58,59] Further analysis of the coordination environment of I^- within $SIPI^-$ structures was performed to evaluate the possibility of transitioning to $CIPI^-$ with TBA^+. The solvation structure was partially dehydrated as TBA^+ was involved. It was found that the predominant SIPI- structure was identified as the partially dehydrated complex $[Zn(H_2O)_5\cdots H_2O\cdots I^-(H_2O)_5\cdot TBA^+]^{2+}$ (Fig. S20, SI). The activation energy for transition from this partially dehydrated $SIPI^-$ structure to $CIPI^-$ was calculated to be 0.41 eV, indicating that such a transition is energetically accessible under the simulated conditions. However, even with TBA^+, the direct conversion from SSIP to $CIPI^-$ structures was thermodynamically unfavorable, indicated by a much higher barrier (1.29 eV), which is approximately three times greater than that of the $SIPI^-$ to $CIPI^-$ transition, with endothermicity (Fig. S21, SI). It was expected that TBAI additives induced the Zn^{2+} solvation environment from SSIP to $SIPI^-$ structures, facilitating a more energetically favorable subsequent transition to $CIPI^-$ ($ZnI(H_2O)^{5+}$), respectively (Table S3, SI). Moreover, we calculated the LUMO energy levels of the solvation structures to compare their reducibility (Fig. 5g). $ZnI(H_2O)_5^+$ has a higher LUMO energy level than $[Zn(H_2O)_6]^{2+}$, indicating that $ZnI(H_2O)_5^+$ is more resistant to reduction than $[Zn(H_2O)_6]^{2+}$. Since electrolyte reduction is a major cause of side reactions, the reduced reducibility of $ZnI(H_2O)_5^+$ relative to $[Zn(H_2O)_6]^{2+}$ is consistent with the experimentally observed suppression of side reactions, as shown in Fig. 4. Finally, our computational results provide supportive insights into how TBAI additives may influence the Zn^{2+} solvation environment. According to a previous report, $ZnI(H_2O)_5^+$ has a lower desolvation energy than $[Zn(H_2O)_6]^{2+}$ because I^- anions in the solvation structure are repulsed by the anode surface during Zn plating[27] (Fig. S22, SI). Despite the ultralow bulk concentration of TBAI, electrochemical reactions are spatially confined to the electrode–electrolyte interface, where localized solvation modulation can significantly influence Zn nucleation and growth behavior. A more detailed understanding can be obtained by considering both thermodynamic and kinetic perspectives. From a thermodynamic perspective, the strong coordination ability of I^- is expected to enable the formation of an alternative local solvation structure, namely $ZnI(H_2O)_5^+$, which is more energetically stable than the $[Zn(H_2O)_6]^{2+}$ structure upon Zn^{2+}–I^- association. Although the overall additive

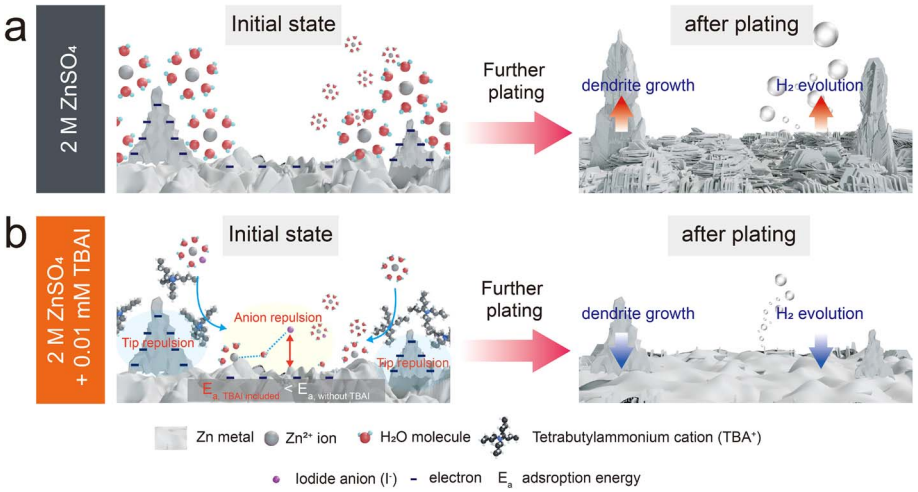

Fig. 6 The schematic of Zn plating patterns in (a) 2 M $ZnSO_4$ electrolyte and (b) 2 M $ZnSO_4$ with 0.01 mM TBAI electrolyte.

concentration remains low, preferential interfacial accumulation of TBA^+ can facilitate local Zn^{2+}–I^- association within the interfacial reaction zone, effectively enriching additive participation at the site where electrochemical reactions occur. The sustained formation of this localized coordination environment persistently modulates the energetics of Zn^{2+} desolvation and reduction at the interface, thereby magnifying the interfacial impact of trace-level TBAI on nucleation behavior and deposition morphology. From a kinetic perspective, the modified solvation structure lowers the effective desolvation barrier and facilitates progressive nucleation behavior. Based on these thermodynamic and kinetic considerations, a schematic illustration is proposed to rationalize the influence of TBAI additives on Zn deposition behavior (Fig. 6). In the additive-free electrolyte, Zn deposition is associated with localized ion flux and uneven growth. In the presence of TBAI, the adsorption of bulky organic cations and the altered solvation environment may collectively contribute to changes in ion redistribution near the electrode surface, which is consistent with the observed suppression of dendritic features. This effect of $[ZnI(H_2O)_5]^+$ contributes to uniform and rapid nucleation without 2D diffusion, as shown in Fig. 2 and S2, SI. Based on the combined experimental observations and computational analyses, a schematic illustration is proposed to rationalize the possible influence of TBAI additives on Zn deposition behavior (Fig. 6). In the additive-free electrolyte, Zn deposition is associated with localized ion flux and uneven growth. In the presence of TBAI, the adsorption of bulky organic cations and the altered solvation environment may collectively contribute to changes in ion redistribution near the electrode surface, which is consistent with the observed suppression of dendritic features.

3.4. Electrochemical performance of a full cell containing the TBAI additive

To evaluate the influence of the TBAI additive under practical full-cell configurations, Zn-based full cells with MnO_2 cathodes (Zn@MnO_2) were assembled and tested. The peaks in the XRD pattern correspond well with the α-MnO_2 structure (PDF 04-055-4884), and the SEM image reveals a characteristic rod-like morphology[40] (Fig. S23, SI). Fig. 7a presents that the Zn@MnO_2 full cell containing 0.01 mM TBAI delivers higher average discharge capacities over a wide range of applied current densities (70 mA g^{-1} to 3.5 A g^{-1}) compared to the additive-free cell. This improvement in rate performance may be associated with the stabilized Zn anode behaviour observed in the presence of TBAI.[41,60,61] Furthermore, the voltage profile of Zn@MnO_2 at various current densities, with and without TBAI (Fig. S24a and b, SI) exhibited no significant difference, suggesting that the introduction of TBAI does not noticeably alter the electrochemical reaction characteristics of the α-MnO_2 cathode. As illustrated in Fig. 7b, Zn@MnO_2 with 0.01 mM TBAI demonstrated stable cycling performance, retaining a specific capacity of 64 mAh g^{-1} and 74.7% capacity retention after 500 cycles at 500 mA g^{-1}. In contrast, the cell without TBAI exhibited rapid capacity fading, maintaining only 37 mAh g^{-1} with 38.9% capacity retention after 500 cycles. Moreover, the discharge voltage profile of Zn@MnO_2 with TBAI exhibited a more stable plateau (~1.4 V), corresponding to the H^+ intercalation reaction, and a better-maintained slope (<1.4 V), associated with Zn^{2+} intercalation, compared to that of the additive-free cell[41] (Fig. S24c and d, SI). These results indicate that the presence of TBAI is associated with improved cycling stability and capacity retention in Zn@MnO_2 full cells.

To further evaluate the practical applicability of TBAI, a full-cell test was conducted using ZVO ($Zn_xV_2O_5 \cdot nH_2O$), a cathode material with higher capacity. The XRD pattern and SEM image are presented in Fig. S25, SI, and are consistent with those from prior study.[42,43] Fig. 7c compares the rate performances of Zn@ZVO full cells with and without TBAI. The Zn@ZVO cell containing TBAI exhibited higher discharge capacities than the additive-free Zn@ZVO cell across a broad range of applied current densities (300 mA g^{-1} to 10 A g^{-1}). The voltage profiles of Zn@ZVO at different current densities remained similar, regardless of TBAI addition (Fig. S26a and b, SI). As Zn@ZVO shows superior rate performance, cycling tests were conducted at a higher current density (5 A g^{-1}) compared to Zn@MnO_2

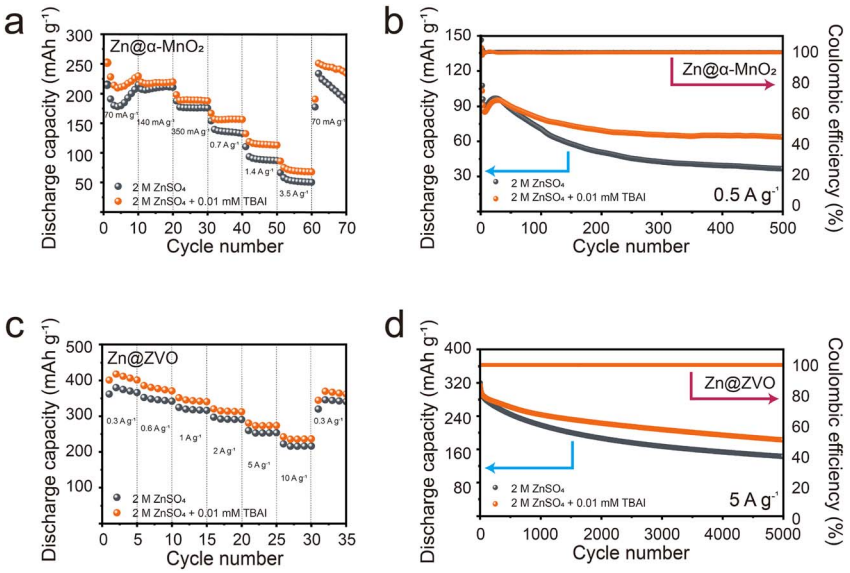

Fig. 7 (a) Rate capability at various current density 70 mA g^{-1} to 3.5 A g^{-1} of Zn@MnO_2 full-cell in different electrolytes. (b) Cycling performance at 500 mA g^{-1} of Zn@MnO_2 full-cell in different electrolytes. (c) Rate capability at various current density 300–10 000 mA g^{-1} of Zn@ZVO full-cell in different electrolytes. (d) Cycling performance at 5 A g^{-1} of Zn@ZVO full-cell in different electrolytes.

(0.5 A g^{-1}). As shown in Fig. 7d, the Zn@ZVO full cell with TBAI exhibited a higher capacity (183 mAh g^{-1}) and capacity retention (58.3%) after 5000 cycles, outperforming the TBAI-free cell, which retained only 143 mAh g^{-1} and 44.7% capacity. The voltage profiles of Zn@ZVO during cycling remained consistent, irrespective of TBAI addition (Fig. S26c and d, SI). To further investigate the electrochemical kinetics at the full-cell level, cyclic voltammetry (CV) measurements were conducted using different cathode systems (Fig. S27). In both Zn@ZVO and Zn@MnO_2 configurations, the TBAI-containing electrolyte exhibits reduced peak separation and an enhanced current response, indicating improved redox kinetics and electrochemical reversibility. These results suggest that the beneficial effect of TBAI originates from the stabilized Zn anode interface rather than cathode-specific behavior.

These electrochemical results further demonstrate that the addition of 0.01 mM TBAI leads to improved capacity retention and cycling stability across different AZIB full-cell systems. Overall, the enhanced rate capability and cycling stability observed in both Zn@MnO_2 and Zn@ZVO full cells indicate that the introduction of TBAI does not compromise cathode electrochemistry, while effectively stabilizing Zn anode behavior under practical full-cell conditions.

4. Conclusion

In this study, the influence of trace-level tetrabutylammonium iodide (TBAI, 0.01 mM) on Zn metal anode behaviour in aqueous Zn-ion batteries was examined. The addition of a small amount of TBAI was found to be associated with more stable Zn plating/stripping behaviour, reduced dendritic features, and suppressed side reactions under the investigated conditions. Compared with additive-free electrolytes, Zn||Zn symmetric cells containing TBAI exhibited prolonged cycling stability, sustaining continuous operation for over 1500 h at 2 mA cm^{-2} and 1 mAh cm^{-2}. When applied to full-cell configurations with α-MnO_2 and $Zn_xV_2O_5$ cathodes, the presence of TBAI was further associated with improved cycling stability and rate capability, without noticeably altering the cathode electrochemical characteristics. These observations suggest that trace-level electrolyte additives can contribute to stabilizing Zn anode behavior in practical aqueous battery systems. Overall, this work highlights the potential of using low-concentration organic cation–halide additives as a simple and scalable strategy to improve Zn metal anode performance, while avoiding complex structural modifications or high additive loadings. The findings provide experimental and computational insights that may be useful for the rational design of electrolyte additives in aqueous Zn-based energy storage systems.

Author contributions

Sang Hyuk Gong, Sunghee Shin, and Hyo Jin Lim: investigation, methodology, writing – original draft; Jin Hwan Kwak: investigation (*in situ* cross-sectional OM); Yisuel Yoo: investigation (DEMS); Insoo Kim: investigation (Raman), writing – original draft (Raman); Puji Lestari Handayani: investigation (DFT), writing – original draft (DFT); U Hyeok Choi: supervision (DFT), writing – review & editing (DFT); Jae Eun Park and Ji Eun Lee: investigation (DFT, MD simulation, RDF), writing – original draft (MD simulation); Seung-Ho Yu: investigation (*in situ* OM), supervision, visualization (*in situ* OM, video), writing – review & editing; Kyung Yoon Chung: investigation, supervision; Sang Kyu Kwak: formal analysis (DFT, MD simulation, RDF), funding acquisition, methodology, supervision, writing – review & editing; Hyung-Seok Kim: conceptualization, funding acquisition, project administration, supervision, writing – review & editing.

Conflicts of interest

There are no conflicts to declare.

Data availability

All data are available upon request from the corresponding author. The data supporting this article have been included as part of the supplementary information (SI). Supplementary information is available. See DOI: https://doi.org/10.1039/d6ta00823b.

Acknowledgements

This work was supported by the National Research Foundation of Korea (NRF) grants and the National Research Council of Science and Technology (NST) grant funded by the Korean Government (MSIT) (No. RS-2024-00407015, RS-2024-00427700 and GTL24011-000). S. K. K. acknowledges computational resources from KITSI (KSC-2024-CRE-0327).

Notes and references

1 N. Liu, X. Wu, Y. Zhang, Y. Yin, C. Sun, Y. Mao, L. Fan and N. Zhang, *Adv. Sci.*, 2020, **7**, 2000146.
2 F. Tang, J. Gao, Q. Ruan, X. Wu, X. Wu, T. Zhang, Z. Liu, Y. Xiang, Z. He and X. Wu, *Electrochim. Acta*, 2020, **353**, 136570.
3 L. E. Blanc, D. Kundu and L. F. Nazar, *Joule*, 2020, **4**, 771–799.
4 E. Levi, Y. Gofer and D. Aurbach, *Chem. Mater.*, 2010, **22**, 860–868.
5 A. Ponrouch, C. Frontera, F. Bardé and M. R. Palacín, *Nat. Mater.*, 2016, **15**, 169–172.
6 D. Yuan, J. Zhao, W. Manalastas Jr, S. Kumar and M. Srinivasan, *Nano Mater. Sci.*, 2020, **2**, 248–263.
7 B. Yong, D. Ma, Y. Wang, H. Mi, C. He and P. Zhang, *Adv. Energy Mater.*, 2020, **10**, 2002354.
8 W. Guo, Z. Cong, Z. Guo, C. Chang, X. Liang, Y. Liu, W. Hu and X. Pu, *Energy Storage Mater.*, 2020, **30**, 104–112.
9 J. Yang, B. Yin, Y. Sun, H. Pan, W. Sun, B. Jia, S. Zhang and T. Ma, *Nano-Micro Lett.*, 2022, **14**, 42.
10 S. Bhoyate, S. Mhin, J.-E. Jeon, K. Park, J. Kim and W. Choi, *ACS Appl. Mater. Interfaces*, 2020, **12**, 27249–27257.
11 Q. Lu, C. Liu, Y. Du, X. Wang, L. Ding, A. Omar and D. Mikhailova, *ACS Appl. Mater. Interfaces*, 2021, **13**, 16869–16875.
12 M. Kwon, J. Lee, S. Ko, G. Lim, S.-H. Yu, J. Hong and M. Lee, *Energy Environ. Sci.*, 2022, **15**, 2889–2899.
13 D. Han, T. Sun, H. Du, Q. Wang, S. Zheng, T. Ma and Z. Tao, *Batteries Supercaps*, 2022, **5**, e202200219.
14 J. Li, Q. Lin, Z. Zheng, L. Cao, W. Lv and Y. Chen, *ACS Appl. Mater. Interfaces*, 2022, **14**, 12323–12330.
15 B. Liu, S. Wang, Z. Wang, H. Lei, Z. Chen and W. Mai, *Small*, 2020, **16**, 2001323.
16 Y. An, Y. Tian, C. Liu, S. Xiong, J. Feng and Y. Qian, *ACS Nano*, 2021, **15**, 15259–15273.
17 H. He and J. Liu, *J. Mater. Chem. A*, 2020, **8**, 22100–22110.
18 M. Wang, Z. Dai, C. Yang, D. Xu, X. Zhang, L. Que, X. Zhang and J. Qin, *Mater. Today Energy*, 2024, **46**, 101736.
19 C. Yang, P. Woottapanit, S. Geng, R. Chanajaree, Y. Shen, K. Lolupiman, W. Limphirat, T. Pakornchote, T. Bovornratanaraks, X. Zhang, J. Qin and Y. Huang, *Nat. Commun.*, 2025, **16**, 183.
20 N. Kiatwisarnkij, Z. Song, C. Tangpongkitjaroen, S. Wannapaiboon, X. Zhang, P. Wangyao and J. Qin, *Batteries Supercaps*, 2025, **8**, e202400727.
21 Y. Ou, Z. Cai, J. Wang, R. Zhan, S. Liu, Z. Lu and Y. Sun, *EcoMat*, 2022, **4**, e12167.
22 L. Shang, C. Cao, J. Fan and L. Yuan, *J. Energy Storage*, 2025, **136**, 118388.
23 W. Xu, K. Zhao, W. Huo, Y. Wang, G. Yao, X. Gu, H. Cheng, L. Mai, C. Hu and X. Wang, *Nano Energy*, 2019, **62**, 275–281.
24 Q. Zhang, J. Luan, L. Fu, S. Wu, Y. Tang, X. Ji and H. Wang, *Angew. Chem., Int. Ed.*, 2019, **58**, 15841–15847.
25 A. Wijitrat, J. Qin, J. Kasemchainan and N. Tantavichet, *J. Ind. Eng. Chem.*, 2022, **112**, 96–105.
26 A. Bayaguud, X. Luo, Y. Fu and C. Zhu, *ACS Energy Lett.*, 2020, **5**, 3012–3020.
27 C. Lan, C. Lee and T.-S. Chin, *Electrochim. Acta*, 2007, **52**, 5407–5416.
28 S. Hosseini, W. Lao-Atiman, S. J. Han, A. Arpornwichanop, T. Yonezawa and S. Kheawhom, *Sci. Rep.*, 2018, **8**, 14909.
29 M. Luo, C. Wang, H. Lu, Y. Lu, B. B. Xu, W. Sun, H. Pan, M. Yan and Y. Jiang, *Energy Storage Mater.*, 2021, **41**, 515–521.
30 N. Wang, S. Zhai, Y. Ma, X. Tan, K. Jiang, W. Zhong, W. Zhang, N. Chen, W. Chen and S. Li, *Energy Storage Mater.*, 2021, **43**, 585–594.
31 Z. Dai, X. Zhang, C. Yang, K. Lolupiman, N. Kiatwisarnkij, X. Zhang and J. Qin, *Adv. Energy Mater.*, 2025, **15**(38), e03193.
32 K. Lolupiman, C. Yang, P. Woottapanit, W. Sukmas, W. Limphirat, N. Rodthongkum, X. Zhang, G. He and J. Qin, *Adv. Funct. Mater.*, 2026, **36**, e24100.
33 P. Woottapanit, C. Yang, S. Geng, K. Lolupimna, W. Limphirat, X. Zhang, G. He and J. Qin, *Adv. Funct. Mater.*, 2025, **35**(46), e2507725.
34 C. Yang, P. Woottapanit, Q. Hou, Z. Dai, W. Limphirat, J. Qin and X. Zhang, *Chem. Commun.*, 2026, **62**, 1409–1426.
35 Y. Wu, L. Wen, S. Wei, J. Shi, Q. Zhou, Q. Zhou, W. Jiang, X. Wu, P. J. Chimtali, Q. Chi, C. Wang and L. Song, *Nanoscale*, 2026, **18**, 2202–2214.
36 A. Behera, D. Deb and A. J. Bhattacharyya, *J. Mater. Chem. A*, 2025, **13**, 33784–33797.
37 Y. Zhu, J. Yin, X. Zheng, A.-H. Emwas, Y. Lei, O. F. Mohammed, Y. Cui and H. N. Alshareef, *Energy Environ. Sci.*, 2021, **14**, 4463–4473.
38 W. Yuan, X. Nie, Y. Wang, X. Li, G. Ma, Y. Wang, S. Shen and N. Zhang, *ACS Nano*, 2023, **17**, 23861–23871.
39 Q. Yue, Y. Chen, J. He, X. Zhu, Y. Wan, L. Qiu, T. Gao, Q. Zhao, D. Xiao and X. Li, *Chem. Eng. J.*, 2025, **510**, 100038.
40 S. Liang, F. Teng, G. Bulgan, R. Zong and Y. Zhu, *J. Phys. Chem. C*, 2008, **112**, 5307–5315.

41 Y. Li, S. Wang, J. R. Salvador, J. Wu, B. Liu, W. Yang, J. Yang, W. Zhang, J. Liu and J. Yang, *Chem. Mater.*, 2019, **31**, 2036–2047.
42 C. Li, A. Shyamsunder, A. G. Hoane, D. M. Long, C. Y. Kwok, P. G. Kotula, K. R. Zavadil, A. A. Gewirth and L. F. Nazar, *Joule*, 2022, **6**, 1103–1120.
43 R. Venkatesan, R. Bauri and K. K. Mayuranathan, *Energy Fuels*, 2022, **36**, 7854–7864.
44 B. Delley, *J. Chem. Phys.*, 1990, **92**, 508–517.
45 B. Delley, *J. Chem. Phys.*, 2000, **113**, 7756–7764.
46 A. D. Becke, *J. Chem. Phys.*, 1993, **98**, 5648–5652.
47 P. J. Stephens, F. J. Devlin, C. F. Chabalowski and M. J. Frisch, *J. Chem. Phys.*, 1994, **98**, 11623–11627.
48 J. Cao, D. Zhang, C. Gu, X. Wang, S. Wang, X. Zhang, J. Qin and Z. S. Wu, *Adv. Energy Mater.*, 2021, **11**, 2101299.
49 H.-Y. Wu, X. Gu, P. Huang, C. Sun, H. Hu, Y. Zhong and C. Lai, *J. Mater. Chem. A*, 2021, **9**, 7025–7033.
50 S. A. Umoren and M. M. Solomon, *J. Ind. Eng. Chem.*, 2015, **21**, 81–100.
51 T. Wang, P. Wang, L. Pan, Z. He, L. Dai, L. Wang, S. Liu, S. C. Jun, B. Lu, S. Liang and J. Zhou, *Adv. Energy Mater.*, 2022, **13**, 2203523.
52 Z. Miao, M. Du, H. Li, F. Zhang, H. Jiang, Y. Sang, Q. Li, H. Liu and S. Wang, *EcoMat*, 2021, **3**, e12125.
53 Y. Li, P. Wu, W. Zhong, C. Xie, Y. Xie, Q. Zhang, D. Sun, Y. Tang and H. Wang, *Energy Environ. Sci.*, 2021, **14**, 5563–5571.
54 Q. Zhang, J. Luan, Y. Tang, X. Ji and H. Wang, *Angew. Chem., Int. Ed.*, 2020, **59**, 13180–13191.
55 D. Feng, F. Cao, L. Hou, T. Li, Y. Jiao and P. Wu, *Small*, 2021, **17**, 2103195.
56 J. Chen, M. Chen, H. Ma, W. Zhou and X. Xu, *Energy Rev.*, 2022, **1**, 100005.
57 Q. Zhang, Y. Ma, Y. Lu, L. Li, F. Wan, K. Zhang and J. Chen, *Nat. Commun.*, 2020, **11**, 4463.
58 Z. Miao, Q. Liu, W. Wei, X. Zhao, M. Du, H. Li, F. Zhang, M. Hao, Z. Cui, Y. Sang, X. Wang, H. Liu and S. Wang, *Nano Energy*, 2022, **97**, 107145.
59 B. Wang, R. Zheng, W. Yang, X. Han, C. Hou, Q. Zhang, Y. Li, K. Li and H. Wang, *Adv. Funct. Mater.*, 2022, **32**, 2112693.
60 W. Du, E. H. Ang, Y. Yang, Y. Zhang, M. Ye and C. C. Li, *Energy Environ. Sci.*, 2020, **13**, 3330–3360.
61 P. Sun, L. Ma, W. Zhou, M. Qiu, Z. Wang, D. Chao and W. Mai, *Angew. Chem., Int. Ed.*, 2021, **60**, 18247–18255.

